Taylor & Francis
Taylor & Francis Group

Automatika

Journal for Control, Measurement, Electronics, Computing and Communications

ISSN: (Print) (Online) Journal homepage: https://www.tandfonline.com/loi/taut20

Robust adaptive backstepping control for a lower-limb exoskeleton system with model uncertainties and external disturbances

Jyotindra Narayan, Mohamed Abbas & Santosha K. Dwivedy

To cite this article: Jyotindra Narayan, Mohamed Abbas & Santosha K. Dwivedy (2023) Robust adaptive backstepping control for a lower-limb exoskeleton system with model uncertainties and external disturbances, Automatika, 64:1, 145-161, DOI: 10.1080/00051144.2022.2119498

To link to this article: https://doi.org/10.1080/00051144.2022.2119498

Published online: 08 Sep 2022.

AUTOMATIKA
2023, VOL. 64, NO. 1, 145–161
https://doi.org/10.1080/00051144.2022.2119498

REGULAR PAPER

OPEN ACCESS Check for updates

Robust adaptive backstepping control for a lower-limb exoskeleton system with model uncertainties and external disturbances

Jyotindra Narayan [a], Mohamed Abbas [a,b] and Santosha K. Dwivedy [a]

[a]Department of Mechanical Engineering, Indian Institute of Technology Guwahati, Guwahati, India; [b]Department of Design and Production, Al-Baath University, Homs, Syria

ABSTRACT

The main purpose of this work is to design a robust adaptive backstepping (RABS) control strategy for a pediatric exoskeleton system during passive-assist gait rehabilitation. The nonlinear dynamics of the exoskeleton system have ill-effects of uncertain parameters and external interferences. In this work, the designed robust control strategy is applied on the exoskeleton to assist children of 08–12 years, 25–40 kg weight, and 115–125 cm height. The dynamic model of the coupled human-exoskeleton system is established using the Euler–Lagrange principle. An appropriate Lyapunov function is selected to prove the uniform boundedness of the control signals. The "explosion of terms" is avoided by establishing a virtual control law without the dynamical system parameters. A Microsoft Kinect-LabVIEW experiment is carried out to estimate the desired gait trajectory. The robustness of the proposed control is validated by varying the limb segment masses and inducing the periodic external disturbances. The proposed control strategy is compared with the decentralized modified simple adaptive-PD (DMSA-PD) control strategy. From simulation results and performance improvement index, it is observed that RABS control outperforms the contrast control (DMSA-PD) to track the desired gait during passive-assist rehabilitation under the effect of model uncertainties and external disturbances.

ARTICLE HISTORY
Received 1 May 2021
Accepted 26 August 2022

KEYWORDS
Lower-limb exoskeleton; robust adaptive backstepping control; model uncertainties; external disturbances; Lyapunov analysis

1. Introduction

The increasing population has witnessed neurological diseases as an emerging challenge in day-to-day life. In most stroke cases, the motor ability of different body extremities deteriorates due to the sudden hampering of blood flow to the brain [1]. As reported by World Health Organization [2], stroke is the second principal reason for the death of more than 5 million people during 2000–2016 and the third leading source of disability worldwide. Among stroke-affected body parts, the lower extremity impairment restricts most daily living activities (ADLs) such as sitting, moving, walking and standing. To amplify the lower extremity's motor performance for stroke patients, traditional rehabilitation training has been performed by physiotherapists [3,4]. As per the clinical research of neurological rehabilitation, the repetitive movement of impaired extremity has shown positive impressions to retrieve the functionality and improve body stability [5,6]. Although physiotherapists can conduct therapeutic measures depending on their skills and experiences, there are certain limitations in the manual process like excessive time consumption, high labour concentration, high training cost, inadequate repeatability, and low sustainability [7]. Therefore, robotic-exoskeleton devices have been introduced in the market to carry out more effective rehabilitation training of the lower extremity by addressing the issues of manual therapy settings [8,9].

For the last two decades, many multi-joint and single-joint-based lower limb exoskeleton devices have been developed for gait rehabilitation, motion assistance, and military strength augmentation [10]. To amplify human endurance while carrying heavy loads, BLEEX [11] was developed with intelligent and adaptable strategies by augmenting robotics capabilities. A treadmill-mounted robotic exoskeleton, LOPES [12], has been introduced to rehabilitate the lower extremity where the hip joint was kept active. Kim et al. [13] developed a 14-DOFs lower-limb exoskeleton to provide gait assistance, having a 3-DOFs hip joint, a 1-DOF knee joint, and a 3-DOFs ankle joint for each limb. Cestari et al. [14] presented the ATLAS exoskeleton to assist the children during flexion/extension of hip, knee, and ankle joints. At the introductory level, a dummy with body features of 10 years human child was used to test the exoskeleton system. In other work on multi-joint exoskeleton devices, Ouyang et al. [15] proposed a hydraulic power unit for the rehabilitation of trunk-hip-knee-ankle-foot (THKAF) while having the advantage of the high power-to-weight ratio. Recently,

CONTACT Jyotindra Narayan n.jyotindra@gmail.com Department of Mechanical Engineering, Indian Institute of Technology Guwahati, Guwahati 781039, India

Tovar-Estrada et al. [16] presented the modelling, simulation, and development of a lower-extremity exoskeleton to assist subjects with neuromuscular debilities in the sagittal, frontal and transverse planes.

The effectiveness of lower limb robotic-based rehabilitation devices can be significantly improved by applying accurate control strategies during training procedures. Control techniques are designed to provide the best possible treatment for the subject while performing repetitive motions. The control of exoskeleton systems presents additional complexity over industrial manipulator control due to the complicated mechanical structure, sophisticated motion, complex trajectory, and human interaction. Trajectory tracking control is considered the foundation of all other control strategies for robotic exoskeletons in the literature. The pre-specified gait trajectory control scheme requires a predefined joint trajectory that could be accessed from different motion-based experiments. The rehabilitation mode of the IHMC exoskeleton also achieves the desired joint angles, as input parameters to the control strategy, from the healthy individuals [17]. In other work on the ReWalk exoskeleton, the trajectory tracking control is designed to achieve the predefined hip and knee joint angular movements [18]. In the ATLAS exoskeleton, the hip and knee joint trajectories are recorded from the healthy children and implemented the position-based phase identification control for the rehabilitation of a quadriplegic girl child [19]. The majority of the exoskeletons utilize healthy humans' predefined gait trajectory for rehabilitation purposes. However, in practice, the precise tracking of the desired gait trajectory is not achieved due to the uncertainties and disturbances of the system dynamics. Therefore, the simple trajectory tracking techniques are improved using intelligent and adaptive laws based on system dynamics.

Furthermore, several intelligent and adaptive control strategies have also been developed for the lower limb exoskeleton system to address these complexities. For instance, a sensitivity amplification control is utilized for BLEEX to track gait trajectory without any sensor sharing between human and exoskeleton [20]. A sliding mode control-based scheme is proposed by Hussain et al. [21] to supervise the lower limb of the individuals for desired trajectories using an orthosis device. Yang et al. [22] presented the second-order command filter along with the conventional backstepping control for the gait exoskeleton system to avoid the "explosion of terms". However, such approaches increase the computational complexity of the controller. Neural Network (NN), in addition to time-delay estimation-based control, is employed by Zhang et al. [23] to achieve the desired trajectory with a virtual prototype of 10-DOF lower limb exoskeleton. The effectiveness of the proposed controller is compared with the conventional PD controller. The heuristic tuning of NN hyperparameters is a cumbersome task for effective model identification. Khan et al. [24] presented a model-free adaptive compliance control for a robotic exoskeleton inspired by reinforcement learning. The performance of the control strategy is visualized with a simulation model. In a work by Gui et al. [25], a model reference adaptive control (MRAC) is designed to regulate the impedance during human-robot interaction in the case of exoskeleton systems. Mokhtari et al. [26] proposed a novel adaptive high-order super-twisting sliding mode control is proposed, accounting for the impedance relationship between the exoskeleton and user. The effectiveness of the proposed control is investigated by comparing it to the optimal sliding mode control. Chen et al. [27] proposed an adaptive backstepping control scheme to enhance the tracking performance of 2-DOF gait exoskeleton where the uncertain model is initially identified using neighbourhood field optimization (NFO) method. However, they have not discussed the complexities of the adaptive backstepping controller. In other work on adaptive control, a new fast terminal sliding mode controller is introduced by Mokhtari et al. [28] to reduce the chattering phenomena and ensure the finite-time convergence. A very recent work on backstepping non-singular fast terminal integral-type sliding mode is carried out for a lower-extremity exoskeleton in active-assist mode [29]. Simulation runs for the proposed control scheme show improved results compared to adaptive non-singular fast terminal integral-type sliding mode control and conventional sliding mode control.

Although several robust control strategies have been developed for the lower extremity exoskeleton, most designs always suffer from the difficulty of selecting an appropriate Lyapunov function, which is fundamentally based on heuristic methods. Furthermore, in the case of pediatric rehabilitation, the parametric uncertainties and un-modeled disturbances become more significant due to substantial variation of dynamic parameters (system mass and length) and body reflexes (unintended subject response). Therefore, to address these benchmark problems, a new robust adaptive backstepping control is designed in this work and implemented on the pediatric exoskeleton system subjected to parametric uncertainties and external disturbances during passive-assist rehabilitation. The proposed control involves a systematic design approach that implicitly constructs the Lyapunov candidate function for exoskeleton dynamics' nonlinear parametric strict-feedback form. The complete design process and stability analysis of RABS control does not require linear input-output dynamics compared to most other control approaches. To the authors' best knowledge, the proposed control has hardly been designed and implemented for the lower-limb exoskeleton systems to

date. The significant contributions of the work are as follows:

(i) A new robust adaptive backstepping (RABS) control is designed for the pediatric lower-limb exoskeleton system in the presence of parametric uncertainties and external disturbances. The proposed design approach inherently addresses the well-known complexities of a common adaptive backstepping control such as "overparameterization" and "explosion of terms" without any filtering approach.

(ii) The convergence of the tracking errors during passive-assist gait rehabilitation is implicitly ensured using a design-based Lyapunov function. This stability proof guarantees the precise alignment of the subject's limbs with the exoskeleton in the presence of uncertain reflexes.

(iii) The effectiveness of the proposed control is investigated by comparing it to a contrast control strategy, named decentralized modified simple adaptive-PD control with and without the varying coupled masses and periodic disturbances.

The remainder of the work is organized as follows. Section 2 presents a brief description of the lower limb exoskeleton system and the computation of the desired gait trajectory. In Section 3, a detailed dynamic analysis of the lower limb exoskeleton model is presented using the Euler–Lagrange principle. In Section 4, adaptive backstepping control design is proposed by implicitly ensuring the Lyapunov stability criterion for uncertain

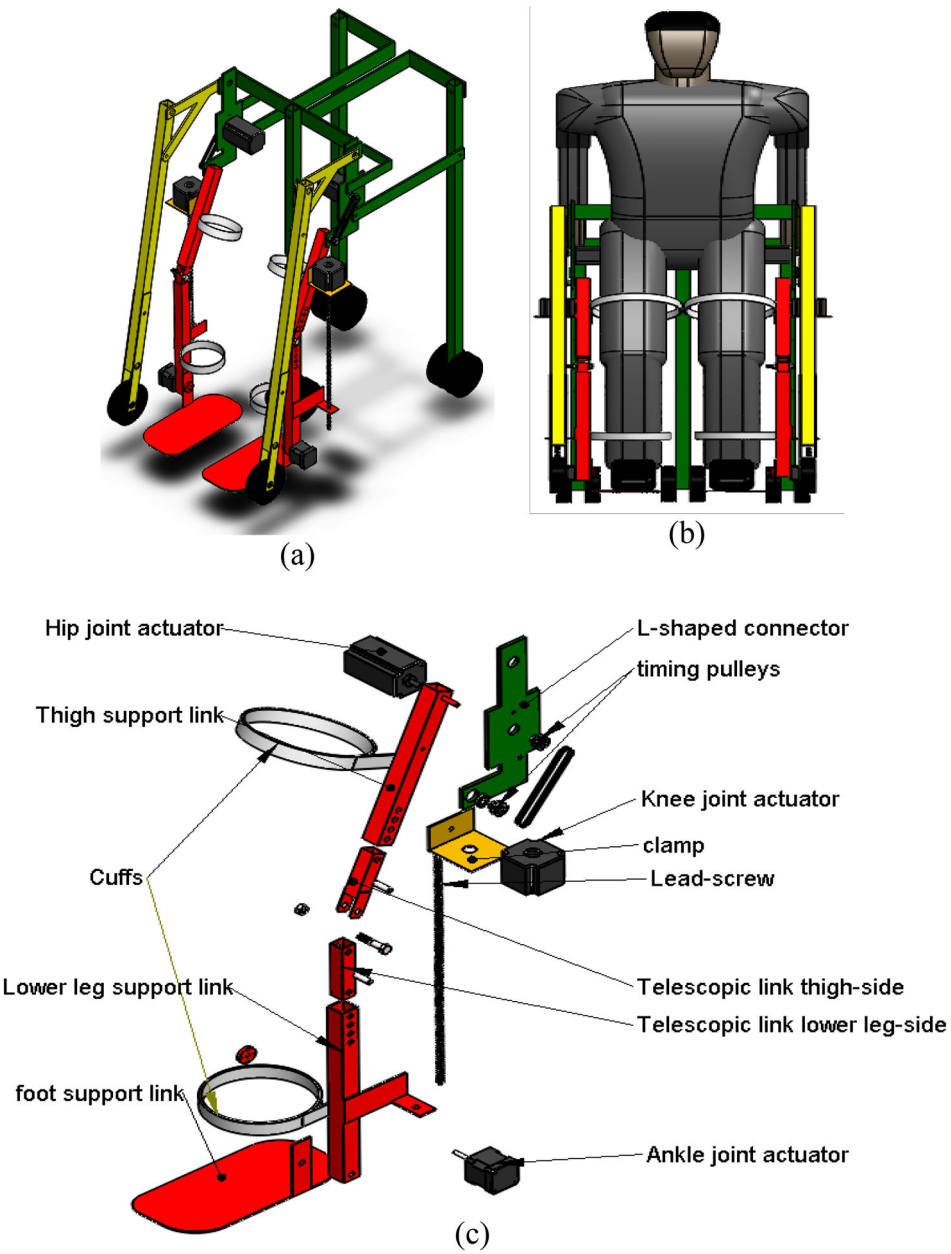

Figure 1. CAD model of (a) LLES, (b) LEES with a human dummy, and (c) LLES's leg in exploded view.

dynamics and undesirable disturbance. Section 5 discusses the details of the experiment setup for the desired gait trajectory and simulation results of the proposed controller with and without parametric variations and external disturbances. In Section 6, the concluding remarks of the complete work are presented.

2. Description of the lower-limb exoskeleton model

While designing a lower limb exoskeleton system for rehabilitation training, the main focus is to confirm the strength and stability of frames, links, and joints. However, retaining the system's strength and keeping the system's overall weight low can only be achieved by having a trade-off between both design criteria. The height adjustability of the different users within a single exoskeleton system should be considered to improve the cost-effectiveness. A specified set of motions, types and placements of the joint actuators need to be correctly designed for the physiological safety of the subject. Furthermore, selecting freedom of movement for different lower limb joints imparts a crucial role in the sustainable design of the lower-limb exoskeleton system. As it could be possible that the subject may feel more comfortable with higher DOFs, considering all possible DOFs for every lower limb joint might lead to uncontrollable movements during the initial phase of therapeutic training. Referring to these design aspects, a 6-DOFs lower-limb exoskeleton system (LLES) from [30] is considered in this work, as shown in Figures 1(a) and (b).

The exploded view of the design with each component is shown in Figure 1(c). The total mass of the LB system, including actuators, is 16 kg. The hip, knee, and ankle joints, each having single freedom of movement, form a 3-DOFs linkage mechanism representing a human leg. The mass and size of each joint are provided in Table 1. Three links, namely, thigh link, calf link, and foot link, are designed and connected via revolute joints for each exoskeleton limb. The masses of the links (including joints and actuators) and respective lengths are mentioned in Table 3 of Section 5. The assigned material of the links and stand-support is the Aluminum alloy. The weight borne by the links is decided as per the maximum transverse load applied at the hip joint during walking. According to van den Bogert et al. [31] and Weinhandl et al. [32], the maximum vertical hip joint force (HJF) varies from 2.2–4.6 times of total body weight (BW) during the single support phase. These loading conditions were estimated using OpenSim's accelerometers [31] or joint reaction algorithm [32]. In this work, assuming the four times of coupled human-exoskeleton weight, the maximum loading at the hip joint can be calculated as $4 \times (m_t^e + m_t^h) \times 9.81 = 4 \times (8 + 40) \times 9.81 = 1920$N, where m_t^e and m_t^h denotes the total weight of exoskeleton links and human subject, respectively. Thereafter, the finite element analysis (FEA) for the hip joint connector is carried out at the expense of 1920N downward force with the hinge-fixed boundary conditions. The Von-Mises stresses are found within the yield limit of the selected material, which further ensures that the dimensional weight of the links is well-acceptable. The detailed design and analysis of the exoskeleton system are already presented in Narayan and Dwivedy [30].

Table 1. Mass and size description of each joint in exoskeleton system.

Joint Name	Mass (kg)	Mechanism/Joint type	Connectors description
Hip	0.35	Timing Belt-Pulley	Pulley outer diameter: 25 mm, centre-to-centre distance: 6 cm, and belt width: 6mm
Knee	0.24	Telescopic-based revolute	Mild steel head screw bolt: M3 × 8mm
Ankle	0.11	Revolute	Hole diameter: 3mm

Hip joint poses flexion/extension (f/e), knee joint executes flexion/extension (f/e), and ankle joint performs dorsiflexion/plantarflexion (d/p) movements in the sagittal plane. The hip joints are driven by a pair of heavy-duty DC stepper motors along with a timing belt-pulley mechanism of transmission ratio 1. The timing belt pulleys are coupled with the shaft of stepper motors for many good reasons. The primary benefit is maintaining a safe distance between the motor shaft and load-bearing shaft without any complex drives, unlike the harmonic ones. This distance ensures the safety of motor shafts in case of sudden shocks generated during rehabilitation measures. Moreover, the mounting of stepper motors in a more accessible location with easy maintenance is also possible due to the distance maintained by the timing belts, which could not be possible with harmonic drives. Timing belts also have the advantage of driving compliance and tolerance of shaft misalignment. On the other hand, harmonic drives suffer from joint flexibility with high elasticity and nonlinear stiffness, which induces the sources of shafts' misalignment [33,34]. The maximum efficiency with harmonic drives varies from 80 to 90% rather than 95–98% of the timing belt drives [35,36]. The manufacturers of harmonic drives are very limited worldwide because of the complex design and manufacturing process. Consequently, the cost of the harmonic driven-motor setup is very high (2100 USD/hip joint) compared to timing belt driven-motor (210 USD/hip joint) and becomes unaffordable for the research conducted by developing countries. The knee joints are actuated with leadscrew stepper motors, attaching at the mid of the calf and thigh link of the exoskeleton model. A set of telescopic thigh and calf links is designed, about the knee joint, to adjust the system's height for different users. A relation between the translational length of

Table 2. Model and characteristic specifications of the joint actuators.

Characteristics → Joint and Motor Model ↓	Armature resistance, $R_m(\Omega)$	Torque sensitivity, $S_m(Nm/A)$	Current, $I_m(A)$	Armature inductance, $L_m(mH)$	Back-EMF constant, $\Xi_e(V/rads^{-1})$	Operating Voltage, V_0 (Volt)	Step angle, A (deg.)	Linear step size, L_s (micron)
Hip (BH86SH156-6204AKS- IP 65)	0.85	2.83	6.2	9.4	0.312	24–140	1.8	-
Knee (BH57SH100-3004LA-TR8)	1.55	0.83	3.1	6.75	0.265	24–48	1.8	40
Ankle (BH42SH47-1504AF)	2.88	0.36	1.5	5.7	0.214	12–24	1.8	-

the leadscrew and knee joint angle is established using the cosine formula. Ankle joints are actuated using a pair of light-duty stepper motors having less rated output. To maintain a fine trade-off among weight, rated torque, system portability, and cost involved, DC stepper motors are selected over hydraulic and pneumatic actuation drives to drive the joints of the exoskeleton system. The model and characteristic specifications of the actuators in the exoskeleton design are shown in Table 2.

The lower limb exoskeleton system is designed for children of 08–12 years, 25–40 kg weight, and 115–125 cm height. The maximum allowable ranges of motion (ROMs) associated with every lower limb joint of the exoskeleton system are as 30°/−12° (f/e), 60°/−10° (f/e), and 13°/−20° (d/p), respectively. A stand-support ensures the structural stability of the coupled human-exoskeleton system during gait rehabilitation. The mechanical structure of the exoskeleton is mounted to a wheeler stand supported at three vertical links (two at the back and one at the centre), as shown in Figure 1. Therefore, the centre of mass of the subject's body can be altered using stand-support to avoid falling. Moreover, it is pertinent to mention that the design and control architecture is dedicated to subjects with pathological gait only and have a Fugl-Meyer Assessment (FMA) score of 1 (i.e. the subject can walk but with deviated trajectory). If required, the subject can adjust their body's centre of mass (COM) to ensure stability during walking. At last, the provision of an emergency shut down option is made at the software interface to avoid any out-of-the-range movement.

3. Dynamic model of the coupled human-exoskeleton system

Dynamic modelling of the coupled human-exoskeleton system is a mathematical representation of applied joint torques with produced angular acceleration. Several methods are well-established in the literature to model the active form of any strategy, such as the Euler–Lagrange principle, Newton-Euler method, Hamilton theory, and Kane approach. However, the Euler–Lagrange principle is widely used to formulate the dynamic model in state-space relations, exploiting the system's energies. The Euler–Lagrange principle [37] is followed in this work to present the dynamical equations of the coupled human-exoskeleton system in the sagittal plane. A three-linkage configuration for the coupled system is depicted along with the interaction dynamics in Figures 2(a) and (b).

A generalized formulation to estimate the joint torques using the Lagrangian L is as follows.

$$\tau = \frac{d}{dt}\left(\frac{\partial L}{\partial \dot{\theta}_i}\right) - \frac{\partial L}{\partial \theta_i} \tag{1}$$

$$L = K - P \tag{2}$$

where

$$K = \sum_{i=1}^{3}\left(\frac{1}{2}m_i v_i^T v_i + \frac{1}{2}\dot{\theta}_i^T I_i \dot{\theta}_i\right) \tag{3}$$

and,

$$P = \sum_{i=1}^{3}(m_i g y_{ci}) \tag{4}$$

The generalized coordinate for the coupled system is denoted by θ_i.In Equation (2), K and P denote the kinetic and potential energy of the i-link. In Equation (3), m_i, v_i, I_i, and $\dot{\theta}_i$ symbolizes the mass, translational speed of centre of mass, inertia, and angular speed of the i-link. In Equation (4), g refers to gravitational acceleration, and y_{ci} signifies distance between the origin and the i-link's centre point directing towards the gravitational vector.

Substituting Equations (3) and (4) into Equation (2) and solving Equation (1), the dynamics of the lower limb exoskeleton system while interacting with the human limb can be expressed in matrix form as below.

$$\tau + \tau_d = M(\theta)\ddot{\theta} + C(\theta,\dot{\theta})\dot{\theta} + G(\theta) + \mathcal{F}(\dot{\theta}) \tag{5}$$

where,

$$\begin{cases} \tau = \tau_{act} + \tau_{eth} + \tau_{hte} \\ M(\theta) = M^e(\theta) + M^h(\theta) \\ C(\theta,\dot{\theta}) = C^e(\theta,\dot{\theta}) + C^h(\theta,\dot{\theta}) \\ G(\theta) = G^e(\theta) + G^h(\theta) \end{cases} \tag{6}$$

$$M(\theta) = \begin{bmatrix} M_{11} & M_{12} & M_{13} \\ M_{21} & M_{22} & M_{23} \\ M_{31} & M_{32} & M_{33} \end{bmatrix},$$

$$C(\theta,\dot{\theta}) = \begin{bmatrix} C_{11} & C_{12} & C_{13} \\ C_{21} & C_{22} & C_{23} \\ C_{31} & C_{32} & C_{33} \end{bmatrix},$$

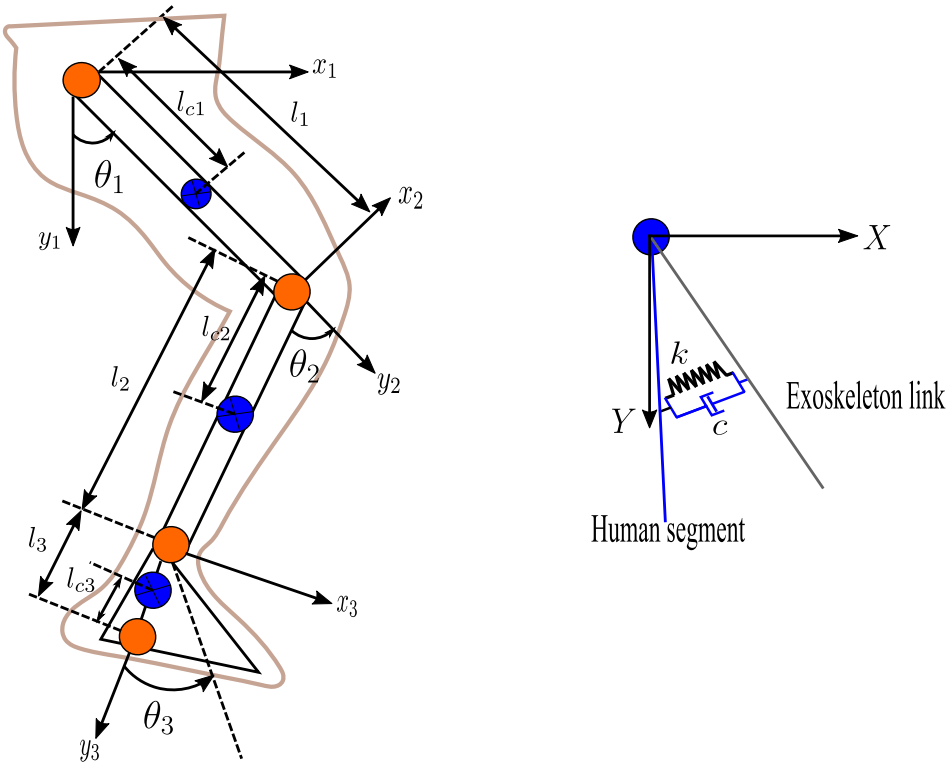

Figure 2. (a) A simplified –linkage coupled human-exoskeleton configuration, and (b) interaction dynamics of coupled human-exoskeleton system.

$$G(\theta) = \begin{bmatrix} G_1 \\ G_2 \\ G_3 \end{bmatrix} \text{ and } \mathcal{F}(\dot{\theta}) = \begin{bmatrix} \mathcal{F}_1 \\ \mathcal{F}_2 \\ \mathcal{F}_3 \end{bmatrix}$$

In Equation (5), $\dot{\theta}$ denotes the joint angular velocity in vector form, and $\ddot{\theta}$ symbolizes the joint angular acceleration in vector form. The disturbance to the system is denoted by τ_d. This could be in the form of un-modeled dynamics and undesirable subjects' responses. $M(\theta), C(\theta, \dot{\theta})$, and $G(\theta)$ signifies the inertial, Coriolis-centrifugal, and gravitational effects of the coupled system in matrix form. The elements of matrices $M(\theta), C(\theta, \dot{\theta})$, and $G(\theta)$ for the coupled system are provided in Appendix A (A1-A3). The friction effects in the exoskeleton system are indicated by $\mathcal{F}(\dot{\theta})$. In Equation (6), $M^e(\theta)$ and $M^h(\theta)$ signify the inertial matrix of the exoskeleton and human limb, respectively. $C^e(\theta, \dot{\theta})$, and $C^h(\theta, \dot{\theta})$ represents the Coriolis-centrifugal matrix of the exoskeleton and human limb, respectively. $G^e(\theta)$ and $G^h(\theta)$ indicate the gravitational effects of the exoskeleton and human limb in matrix form, respectively.τ_{act} denotes the torque of the joint actuator of the coupled system. The interaction torque from exoskeleton limb to a human leg and a human leg to exoskeleton limb is referred by τ_{eth} and τ_{hte}, respectively.

The friction model $\mathcal{F}(\dot{\theta})$, which includes the effects of Coulomb friction ($\text{Ç}_{\mathcal{F}}$) and viscous friction ($\mathcal{V}_{\mathcal{F}}$), are given as:

$$\mathcal{F}(\dot{\theta}) = \text{Ç}_{\mathcal{F}} sgn(\dot{\theta}) + \mathcal{V}_{\mathcal{F}} = \text{Ç}_{\mathcal{F}} sgn(\dot{\theta}) + \sigma\dot{\theta}, \forall\dot{\theta} \neq 0 \tag{7}$$

where σ denotes the angular velocity factor in Nm/rad^{-1}, and *sgn* signifies the signum function.

The interaction torques, τ_{eth}, and τ_{hte} are induced by the link attachments of the human leg and exoskeleton limb using the splints. In this work, the interactions are supposed to be annulled with each other by considering the connections rigid and joint angles to be the same for human and exoskeleton lower limb joints during gait rehabilitation. Therefore, establishing through the interaction dynamics shown in Figure 2(b), the model for the interaction torques are as follows:

$$\begin{aligned} \tau_{eth} = -\tau_{hte} = J^T f_{int} = J^T(k\Delta x + c\Delta\dot{x}) \\ = k(\theta_h - \theta_e) + c(\dot{\theta}_h - \dot{\theta}_e) \end{aligned} \tag{8}$$

where, f_{int} denotes the interaction force between the human and exoskeleton, k and c represents the stiffness and damping coefficients of the splints, Δx signifies the deviation between the human leg and exoskeleton limb in Cartesian coordinates, and $(\theta_h - \theta_e)$ indicates joint angular deviation between the human leg and exoskeleton limb.

The dynamic model, presented in Equation (6), satisfies the following important mathematical properties in matrix form [37].

Properties

(i) $M(\theta)$ poses symmetric as well as definite positive behaviour in the matrix form and holds the

following relation

$$\sim a_1||\beta^2|| \leq \beta^T M(\theta)\beta \leq \sim a_2||\beta^2|| \quad \forall\beta \in \mathcal{R}^3 \tag{9}$$

where, $\sim a_1$ and $\sim a_2$ are positive constants.

(ii) $\dot{M}(\theta) - 2C(\theta,\dot{\theta})$ holds behaviour of skew-symmetric matrix when $\forall\Gamma \in \mathcal{R}^3$,

$$\Gamma^T(\dot{M}(\theta) - 2C(\theta,\dot{\theta}))\Gamma = 0 \tag{10}$$

Assumption

The external disturbances are bounded in such a way to confirm the following condition:

$$||\tau_d|| \leq \bar{\tau}_d \tag{11}$$

where, $\bar{\tau}_d$ denotes a positive constant.

4. Adaptive backstepping control design for exoskeleton system

In this section, the concept of adaptive backstepping [38] is exploited to design the robust structure of trajectory tracking control for the lower limb exoskeleton system during passive-assist rehabilitation. The proposed design is dedicated to controlling the human gait using the exoskeleton system, with dynamic uncertainties and subject response-based external disturbances. Moreover, the Lyapunov theorem is implicitly proved to confirm the stability of the control design. The dynamic model of a simplified *3*-joint lower limb robotic exoskeleton in parametric-based strict-feedback representation can be expressed below.

$$r_1 = \theta, r_2 = \dot{\theta},\ r = [r_1 r_2\ ]^T \tag{12}$$

$$\begin{cases} \dot{r_1} = r_2 \\ \dot{r_2} = M^{-1}(\theta)(\tau + \tau_d - C(\theta,\dot{\theta})\dot{\theta} - G(\theta) - \mathcal{F}(\dot{\theta})) \\ = M^{-1}(\theta)(\tau_{act} + \tau_d - C(\theta,\dot{\theta})\dot{\theta} - G(\theta) - \mathcal{F}(\dot{\theta})) \end{cases} \tag{13}$$

where, $r_1 = [\theta_1,\theta_2,\theta_3]^T, r_2 = [\dot{\theta}_1,\dot{\theta}_2,\dot{\theta}_3]^T \in \mathcal{R}^3$ denote the state vectors of the exoskeleton dynamical system.

The error variables could be outlined as given below:

$$e_1 = \theta - \theta_d = r_1 - \theta_d \tag{14}$$

$$e_2 = \dot{\theta} - \zeta - \dot{\theta}_d = r_2 - \zeta - \dot{\theta}_d \tag{15}$$

where ζ signifies the virtual control law in backstepping design while stabilizing the subsystems. The objective is to guarantee the tracking of the desired angular trajectory θ_d by the actual angular vector θ in the presence of unknown model parameters and undesirable external disturbances. Therefore, the following stepwise process can be employed for the design of adaptive backstepping control.

Step 1:

The derivative of the first error variable $\dot{e}_1$ could be explained in terms of the second error e_2 and virtual control parameter ζ, as follows:

$$\dot{e}_1 = \dot{r}_1 - \dot{\theta}_d = r_2 - \dot{\theta}_d = e_2 + \zeta \tag{16}$$

The virtual control law ζ is supposed to be chosen to stabilize the first error of the subsystem in Equation (16). Consequently, the Lyapunov function candidate can be selected as:

$$\mathcal{T}_1 = \frac{1}{2}({e_1}^T e_1) \tag{17}$$

Substituting Equation (16) after differentiation of Equation (17), the derivative of the Lyapunov function can be obtained as:

$$\dot{\mathcal{T}}_1 = {e_1}^T\dot{e}_1 = {e_1}^T e_2 + {e_1}^T\zeta \tag{18}$$

The virtual control law ζ can be defined as:

$$\zeta = -\varepsilon_1 e_1 = -\varepsilon_1 r_1 + \varepsilon_1\theta_d \tag{19}$$

where, ε_1 is characterized by a diagonal matrix of positive value.

Now, from Equations (18) and (19),

$$\dot{\mathcal{T}}_1 = -{e_1}^T\varepsilon_1 e_1 + {e_1}^T e_2 \tag{20}$$

From Equation (20), it is evident that $\dot{\mathcal{T}}_1$ is negative definite for $e_2 = 0$ and therefore, the first error variable is ensured to be converging.

Step 2:

The derivative of the second error variable $\dot{e}_2$ can be described as follows:

$$\begin{aligned} \dot{e}_2 &= \dot{r}_2 - \dot{\zeta} - \ddot{\theta}_d \\ &= M^{-1}(\theta)(\tau_{act} + \tau_d - C(\theta,\dot{\theta})\dot{\theta} \\ &\quad - G(\theta) - \mathcal{F}(\dot{\theta})) - \dot{\zeta} - \ddot{\theta}_d \end{aligned} \tag{21}$$

where,

$$\dot{\zeta} = -\varepsilon_1\dot{r}_1 + \varepsilon_1\dot{\theta}_d = -\varepsilon_1 r_2 + \varepsilon_1\dot{\theta}_d \tag{22}$$

The appropriate Lyapunov function candidate, constructed on the **property** (i) from Equation (9), can be selected as:

$$\bar{\mathcal{T}}_2 = \mathcal{T}_1 + \mathcal{T}_2 = \mathcal{T}_1 + \frac{1}{2}({e_2}^T M(\theta)e_2) \tag{23}$$

The derivative of the Lyapunov function defined in Equation (23) can be evaluated as:

$$\dot{\bar{\mathcal{T}}}_2 = \dot{\mathcal{T}}_1 + {e_2}^T M(\theta)\dot{e}_2 + \frac{1}{2}{e_2}^T\left(\frac{d(M(\theta))}{dt}\right)e_2 \tag{24}$$

Furthermore, exploiting the **property** (ii) from Equation (10), the second Lyapunov function holds the

derivative form as below:

$$\dot{\mathcal{T}}_2 = \dot{\mathcal{T}}_1 + {e_2}^T(M(\theta)\dot{e}_2 + C(\theta,\dot{\theta})e_2) \tag{25}$$

Based on Equations (15) and (21), the expression $M(\theta)\dot{e}_2 + C(\theta,\dot{\theta})e_2$ from Equation (25) can be represented as:

$$\begin{aligned} M(\theta)\dot{e}_2 + C(\theta,\dot{\theta})e_2 &= M(\theta)\left(r_2 - \dot{\zeta} - \ddot{\theta}_d\right) \\ &\quad + C(\theta,\dot{\theta})(r_2 - \zeta - \dot{\theta}_d) \\ &= M(\theta)\left(-\dot{\zeta} - \ddot{\theta}_d\right) \\ &\quad + C(\theta,\dot{\theta})(-\zeta - \dot{\theta}_d) + \tau_{act} + \tau_d \\ &\quad - G(\theta) - \mathcal{F}(\dot{\theta}) \end{aligned} \tag{26}$$

However, the dynamic parameters in the experimental model of the lower limb exoskeleton system are not precisely known, and the matrices in Equation (26) cannot be applied in the design of the control strategy. Therefore, the direct adaptation law is practiced to assess the unknown dynamic parameters. The right-hand side of Equation (26), representing the unknown model parameters, can be rearranged as follows:

$$\begin{aligned} &M(\theta)\left(-\dot{\zeta} - \ddot{\theta}_d\right) + C(\theta,\dot{\theta})(-\zeta - \dot{\theta}_d) \\ &\quad + \tau_{act} + \tau_d - G(\theta) - \mathcal{F}(\dot{\theta}) \\ &= \Psi\Omega + \tau_{act} + \tau_d \end{aligned} \tag{27}$$

Thereafter, Equation (25) can be rewritten as:

$$\dot{\bar{\mathcal{T}}}_2 = \dot{\mathcal{T}}_1 + {e_2}^T(\Psi\Omega + \tau_{act} + \tau_d) \tag{28}$$

where, $\Psi \in \mathcal{R}^{3\times p}$ refers to a smooth function available from the sensor-based feedback, and $\Omega \in \mathcal{R}^p$ denotes unknown nonlinear parameters. As per the earlier discussion, the Lyapunov function from Equation (23) can be revised as given below:

$$\mathcal{T} = \bar{\mathcal{T}}_2 + \frac{1}{2}\tilde{\Omega}\sqcap^{-1}\tilde{\Omega}; \tilde{\Omega} = \Omega - \breve{\Omega} \tag{29}$$

where estimation of the unknown parameters in matrix form is indicated by $\breve{\Omega}$ and $\sqcap$ denotes an arbitrary selected positive definite matrix.

Now, one may get the following expression after differentiating Equation (29),

$$\begin{aligned} \dot{\mathcal{T}} &= \dot{\bar{\mathcal{T}}}_2 - \tilde{\Omega}^T\sqcap^{-1}\dot{\breve{\Omega}} \\ &= \dot{\mathcal{T}}_1 + {e_2}^T(\Psi\Omega + \tau_{act} + \tau_d) - \tilde{\Omega}^T\sqcap^{-1}\dot{\breve{\Omega}} \end{aligned} \tag{30}$$

By performing addition and subtraction of the term ${e_2}^T\Psi\breve{\Omega}$ to the right-hand side of Equation (30),

$$\begin{aligned} \dot{\mathcal{T}} &= \dot{\mathcal{T}}_1 + {e_2}^T\Psi\breve{\Omega} + {e_2}^T\Psi\tilde{\Omega} \\ &\quad + {e_2}^T(\tau_{act} + \tau_d) - \tilde{\Omega}^T\sqcap^{-1}\dot{\breve{\Omega}} \end{aligned} \tag{31}$$

With the transpose of ${e_2}^T\Psi\ \tilde{\Omega}$, Equation (31) can be rewritten as:

$$\begin{aligned} \dot{\mathcal{T}} &= \dot{\mathcal{T}}_1 + {e_2}^T\Psi\breve{\Omega} + {e_2}^T(\tau_{act} + \tau_d) \\ &\quad + \tilde{\Omega}^T\left(\Psi^T e_2 - \sqcap^{-1}\dot{\breve{\Omega}}\right) \end{aligned} \tag{32}$$

Now by selecting $\dot{\breve{\Omega}}$ as follows:

$$\dot{\breve{\Omega}} = \sqcap\Psi^T e_2 \tag{33}$$

After incorporating Equations (33) and (20) into Equation (32), the derivative of the Lyapunov function can be modified as:

$$\begin{aligned} \dot{\mathcal{T}} &= \dot{\mathcal{T}}_1 + {e_2}^T\Psi\breve{\Omega} + {e_2}^T(\tau_{act} + \tau_d) \\ &= -{e_1}^T\varepsilon_1 e_1 + {e_1}^T e_2 + {e_2}^T\Psi\breve{\Omega} + {e_2}^T\tau_{act} + {e_2}^T\tau_d \end{aligned} \tag{34}$$

Considering **Assumption** (Equation (11)) and employing the Young inequality, the last term on the right-hand side of Equation (34) can be articulated as below:

$$\begin{aligned} {e_2}^T\tau_d &\le \frac{1}{2}{e_2}^T e_2 + \frac{1}{2}{\tau_d}^T\tau_d \\ &\le \frac{1}{2}{e_2}^T e_2 + \frac{1}{2}\bar{\tau}_d^2 \end{aligned} \tag{35}$$

Thereafter, the derivative of the Lyapunov function fulfils the inequality equation as follows:

$$\begin{aligned} \dot{\mathcal{T}} &\le -{e_1}^T\varepsilon_1 e_1 + {e_1}^T e_2 + {e_2}^T\Psi\breve{\Omega} + {e_2}^T\tau_{act} \\ &\quad + \frac{1}{2}{e_2}^T e_2 + \frac{1}{2}\bar{\tau}_d^2 \end{aligned} \tag{36}$$

The trajectory tracking control law can be designed as:

$$\tau_{act} = -\varepsilon_2 e_2 - e_1 - \Psi\breve{\Omega} - \frac{1}{2}e_2 \tag{37}$$

where, ε_2 denotes another diagonal matrix of positive value.

Furthermore, after placing the position control law from Equation (37) to Equation (36), the derivative of the Lyapunov function can be reworked as:

$$\dot{\mathcal{T}} \le -{e_1}^T\varepsilon_1 e_1 - {e_2}^T\varepsilon_2 e_2 + \frac{1}{2}\bar{\tau}_d^2 \tag{38}$$

It is evident from Equation (38) the derivative of the Lyapunov function can be expressed in the following form of inequality,

$$\dot{\mathcal{T}} \le -\mho\mathcal{T} + \rho \tag{39}$$

where,

$$\mho = \min\left(2\lambda_{min}(\varepsilon_1), \frac{2\lambda_{\min}(\varepsilon_2)}{\lambda_{\max}(M(\theta))}\right) \text{ and } \rho = \frac{1}{2}\bar{\tau}_d^2 \tag{40}$$

where ρ belongs to a class of κ functions and $\lambda_{\min}(.)$, $\lambda_{\max}(.)$ are the minimum and maximum eigenvalues of (.), respectively.

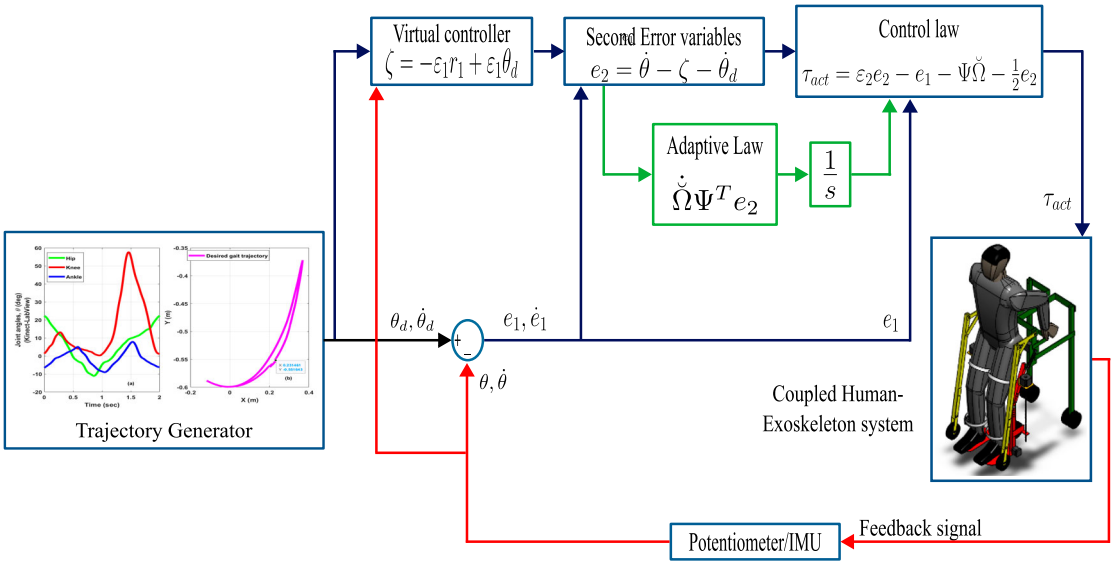

Figure 3. Schematic architecture of robust adaptive backstepping control strategy for the exoskeleton system.

Multiplying both sides of Equations (39) by an exponent term $e^{\mho t}$, the following equation can be obtained:

$$\frac{d}{dt}(\mathcal{T}e^{\mho t}) \leq \rho e^{\mho t} \tag{41}$$

The integration of Equation (41) over $t = [0, t]$ yields:

$$0 \leq \mathcal{T} \leq \left(\mathcal{T}(0) - \frac{\rho}{\mho}\right)e^{-\mho t} + \frac{\rho}{\mho} \tag{42}$$

By defining $\widehat{\mathcal{T}} = \max\{\mathcal{T}(0), (\rho/\mho)\}$, the following inequalities can be achieved:

$$||e_1|| \leq \sqrt{2\,\widehat{\mathcal{T}}}, \text{ and } e_2 \leq \sqrt{\frac{2\,\widehat{\mathcal{T}}}{\lambda_{\max}(M(\theta))}} \text{ and} \tag{43}$$

Remark 1: It is observed from Equations (41–43) that is increasing the $\mho$ and decreasing ρ can ensure the error signals e_1 and e_2 to converge to small values. Consequently, when the controller gains ε_1 and ε_2 are increased, the tracking performance can be improved with reduced positional errors. On the other hand, increasing the adaptation gain $\sqcap$ confirms the fast convergence of the estimated parameters to the actual values. However, in a real-case scenario, the controller parameters cannot be selected as very large to avoid the noise and high frequency, which degrade the system performance.

The above set of equations confirms the characterization of input to state stability (ISS), where input is regarded as the bounded external disturbances $\bar{\tau}_d$, and the proposed control strategy eventually guarantees all the signals to be bounded [39]. In addition, the convergence of even small tracking errors for the coupled human-exoskeleton system can be ensured with the proper selection of control law parameters. The complete design architecture of the robust adaptive backstepping control for the lower limb exoskeleton system is shown in Figure 3. In the closed-loop control, the actual signals from the dynamics can be recorded by using feedback sensors such as potentiometers or inertial motion units (IMUs).

Remark 2: In the parametric strict feedback system, the "overparameterization" problem persists due to the number of parameters' estimates greater than the number of unknown parameters. The reason behind this condition is the presence of unknown parameter estimates in each design step of the adaptive backstepping. However, in the present work, the first design step is free from any unknown parameters estimation and generically postponed to the last design step; therefore, avoiding the "overparameterization" phenomena (refer to **Step 2**). Furthermore, the "explosion of terms" is another well-known complexity that appears from the presence of inertial, centrifugal, and gravity matrices while differentiating the virtual control. However, the proposed design in this work avoids this complexity due to the non-existence of such dynamical matrices (refer to Equation 22).

5. Results and discussion

In this section, the results and observations regarding the performance of the robust adaptive backstepping control are discussed for the lower limb exoskeleton system. The proposed control strategy is exploited to track the desired gait trajectory during passive-assist gait rehabilitation in the presence of model uncertainties and external disturbances. Thereafter, the effectiveness of the designed control strategy is validated with the contrast control strategy (DMSA-PD). The input parameters to both the control strategies are length, weight, and joint angles of lower limb segments for a human child (10 years old, 28 kg weight, and 120 cm height).

Table 3. Specifications of lower limb exoskeleton system and child dummy.

Lower Limb Exoskeleton System			
Part	Mass (Kg)	Length (m)	COM (m)
Thigh link	m_1^e =3.75	l_1^e =0.25-0.30	l_{c1}^e =0.12-0.15
Shank link	m_2^e =1.60	l_2^e =0.30-0.35	l_{c2}^e =0.14-0.17
Foot link	m_3^e =0.85	l_3^e =0.05	l_{c3}^e =0.02
Child (Age 10 years, body weight 28 kg, body height 120 cm)			
Part	Mass (Kg)	Length (m)	COM (m)
Thigh	m_1^h =3.50	l_1^h =0.25	l_{c1}^h =0.12
Shank	m_2^h =2.25	l_2^h =0.30	l_{c2}^h =0.15
Foot	m_3^h =0.65	l_3^h =0.04	l_{c3}^h =0.02

5.1. Input parameters

The lower limb's weight and height parameters for the human child and exoskeleton are enlisted in Table 3. The length of the thigh and shank link of the exoskeleton can be adjusted to accommodate different lower limb segment lengths of children. However, in this work, these lengths are fixed at 25 and 30 cm for the considered child subject of body height 120 cm.

The desired joint angles with the child's respective gait trajectory are estimated using a wireless Kinect-based NI-LabVIEW experimental model. Microsoft Kinect (MS) depth sensor was installed as a motion-capture (MOCAP) device in the institute laboratory to perform the experiment. The MS Kinect comprises an RGB camera, an infrared (IR) emitter, an infrared depth sensor, a tilt motor, an array of four microphones, and a 3-axis accelerometer. The tilt motor is used to adjust the field of view (FOV) settings of the MS Kinect camera. The detailed resolution specifications of the depth camera are given in Narayan and Dwivedy [40]. Thereafter, with necessary permission, the healthy child is asked to walk on a marked path in front of the MS Kinect depth camera. The complete algorithm for the gait analysis experiment is shown in Figure 4(a), and the child skeleton model is shown in Figure 4(b) while performing the motion experiment. The distance between the device's centre and the subject's starting position was 0.7 and 2.2 m in the horizontal and vertical direction, respectively, as shown in Figure 4(c).

The skeleton model is generated, and corresponding information is stored in body joint triples. Configuring the depth sensor with the NI-LabVIEW interface, the joint evaluation block is designed to evaluate the joint angles in the sagittal plane based on the Euclidean distance law and cosine formula. The lower-limb joint trajectories and corresponding desired gait trajectory are shown in Figures 5(a) and (b), respectively. The ROM for hip, knee, and ankle joints are recorded as 22.36° to −9.38°, 58.16° to 1.11°, and 5.34° to −8.04° for a 10-year child, respectively.

5.2. Simulation results

In order to validate the robustness of the proposed control scheme (RABSC), two cases are considered: the first one without model uncertainty and external disturbance (w/o-MUED) and the second with model uncertainty and external disturbance (w-MUED). In the second case, the coupled human-exoskeleton mass of lower limb segments is increased by 30%, 20%, and 10% ($m_1' = m_1 + 0.3m_1, m_2' = m_2 + 0.2m_2, m_3' = m_3 + 0.1m_3$) respectively. Moreover, external disturbances are added as $\mathcal{D}_1 = 6\sin(4\pi t), \mathcal{D}_2 = 5\sin(3\pi t), \mathcal{D}_3 = 3\sin(2\pi t)$. In this work, a periodic (sinusoidal) form of external disturbances is added to mimic the effect of sudden reflexes induced at the joints throughout a gait cycle. These reflexes are caused due to the pathological gait (altered one) in the case of post-stroke subjects. After performing numerical iterations, the control law parameters are selected as $\boldsymbol{\varepsilon}_1 = diag(175, 175, 175), \boldsymbol{\varepsilon}_2 = diag(70, 70, 70)$, and $\sqcap = diag(0.06, 0.06, 0.06)$.

By incorporating kinematic, dynamic, and control law parameters in the robust adaptive backstepping control (w/o-MUED and w-MUED), the trajectory tracking of the desired gait is presented in Figure 6. A gait cycle is considered to be completed in 2 s. The black line represents the desired trajectory starting with (X: 0.23 m, Y: −0.56 m). The actual trajectories after applying the proposed control (RABS) are shown by the dotted red line (w/o-MUED) and the blue line (w-MUED). A zoomed-in view is shown at (X, Y: 0, −0.599; 0, 0.1) to distinguish between the desired and the actual trajectory. The position error in X- and Y-direction (e_x and e_y) is shown in Figures 7(a) and (b). Considering the system without model uncertainties and external disturbances, the maximum absolute deviation from the desired trajectory in X-direction ($|e_x|_{\max}$) is 0.125 m. On the other hand, considering the model uncertainties and external disturbances in the system, the respective deviation is 0.127 m. The maximum absolute deviation in Y-direction ($|e_y|_{\max}$) for both the cases is recorded as 0.009 m (w/o-MUED) and 0.01 m (w-MUED).

The tracking of desired joint angles of the lower limb is shown in Figures 8(a)–(c). To visualize the difference between desired joint angles and controlled joint angles, a zoomed-in view is illustrated at 75% of the gait cycle (1.5s). Figure 9(a)–(c) represents the error ($e_{\theta H}, e_{\theta K}$, and $e_{\theta A}$) between desired and actual joint trajectory. In the case of the hip joint, the maximum absolute deviation ($|e_{\theta H}|_{max}$) from the desired joint trajectory for both the cases is 0.64° (w/o-MUED) and 0.67° (w-MUED). The maximum absolute deviation ($|e_{\theta K}|_{\max}$) in the case of the knee joint is recorded as 2.04° and 2.01° for the system without MUED and with MUED, respectively. The respective deviations

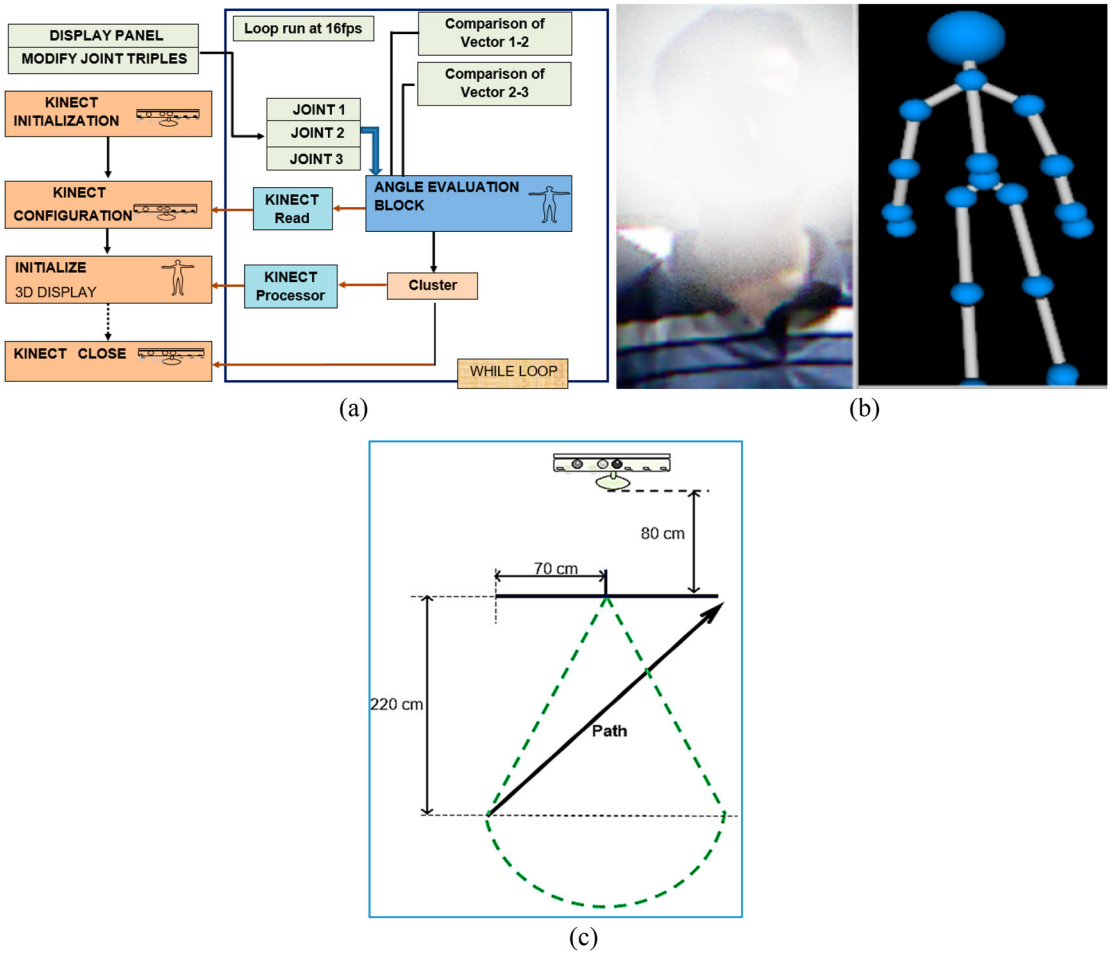

Figure 4. (a) Joint evaluation algorithm using Kinect-LabVIEW setup, (b) child participant along with his skeleton image during gait analysis, and (c) path setup in experimental setting [40].

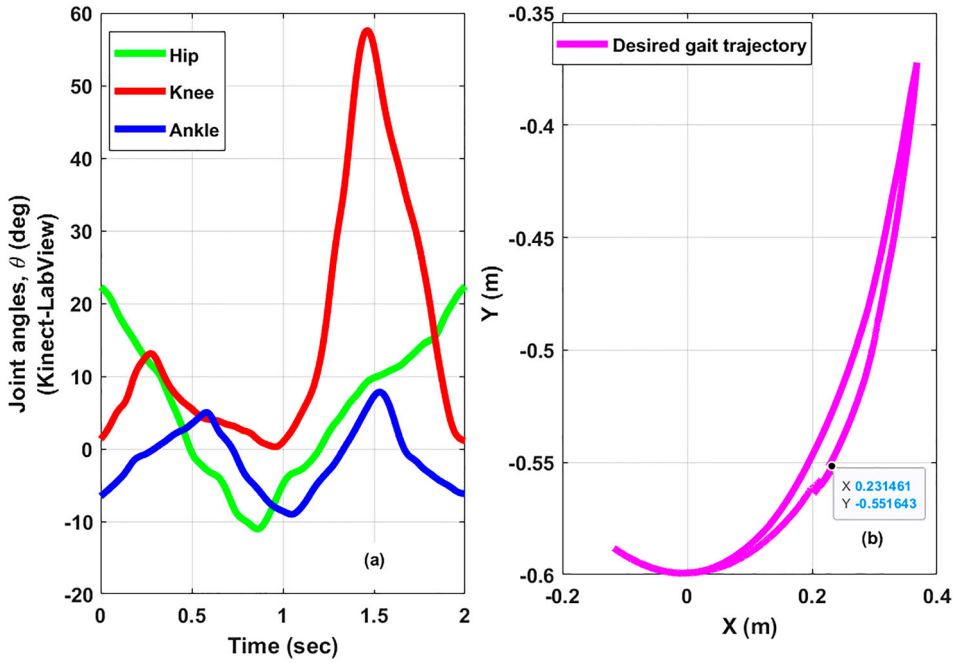

Figure 5. (a) Desired joint trajectories, and (b) desired gait trajectory of the 10 year child.

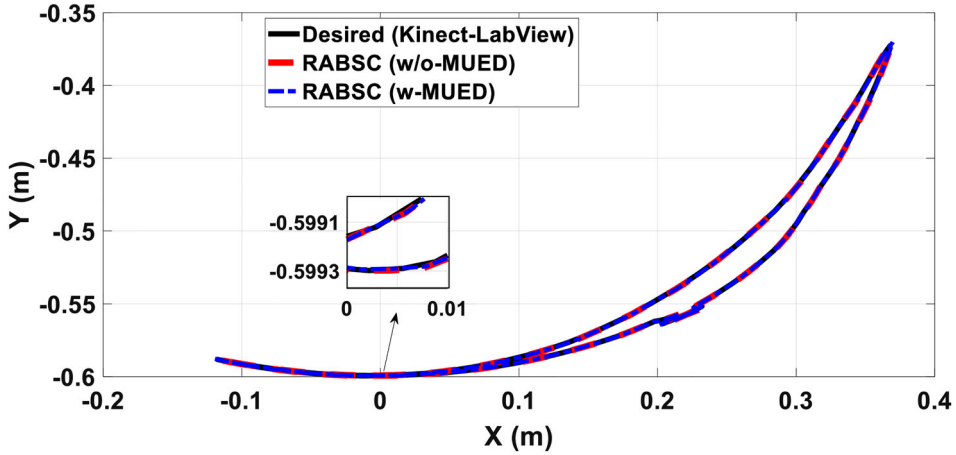

Figure 6. Simulation results of desired trajectory tracking for proposed control without and with model uncertainties and external disturbances.

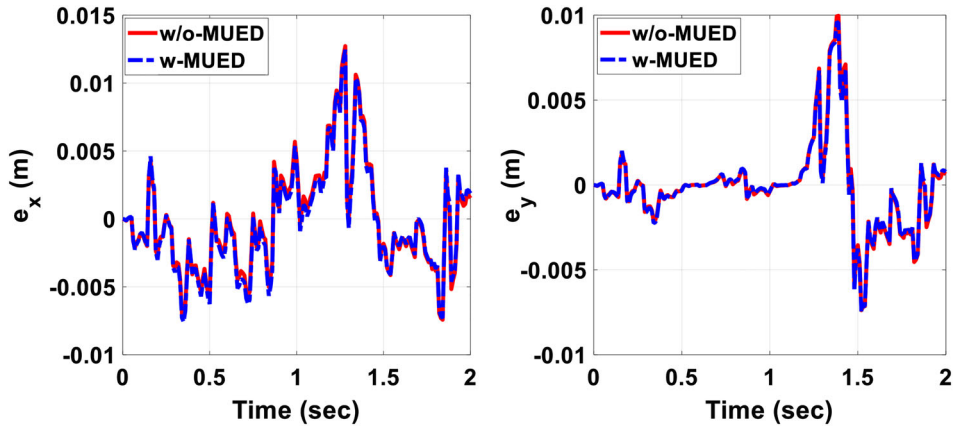

Figure 7. Simulation results of position tracking error for proposed control without and with MUED in (a) X-direction, and (b) Y-direction.

for ankle joint ($|e_{\theta A}|_{\max}$) are found to be 0.71° and 0.72°.

While tracking the desired gait trajectory during passive-assist gait rehabilitation, the control torques ($\boldsymbol{\tau}_H, \boldsymbol{\tau}_K$, and $\boldsymbol{\tau}_A$) for both the cases are estimated and shown in Figure 10(a)–(c). Considering the first case (w/o-MUED), the maximum control torques for hip, knee, and ankle joints are evaluated as 24.92, 13.71, and 3.97 Nm. On the other hand, the respective control torques for the second case (w-MUED) are computed as 25.72, 13.42, and 4.11 Nm. It can be observed from the position and angular tracking results that there is an insignificant difference between the two considered cases (w/o-MUED and w-MUED) for the proposed

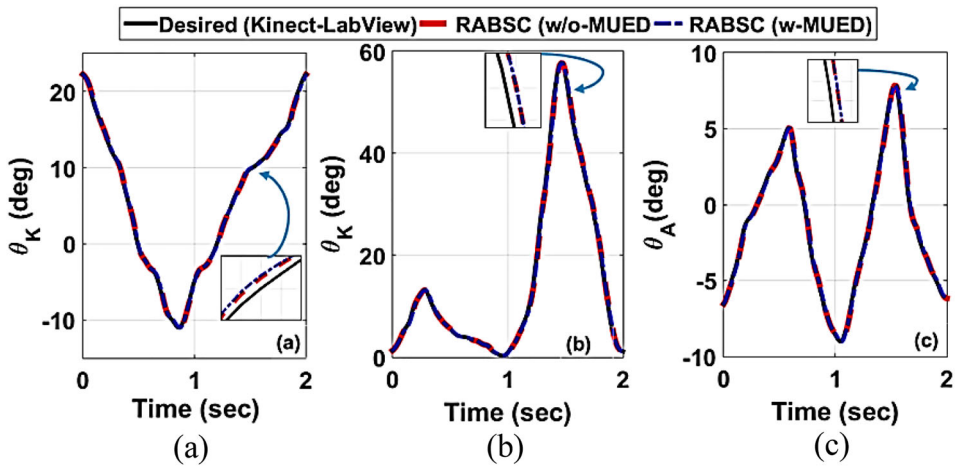

Figure 8. Simulation results of (a) hip, (b) knee, and (c) ankle joint tracking for proposed control without and with MUED.

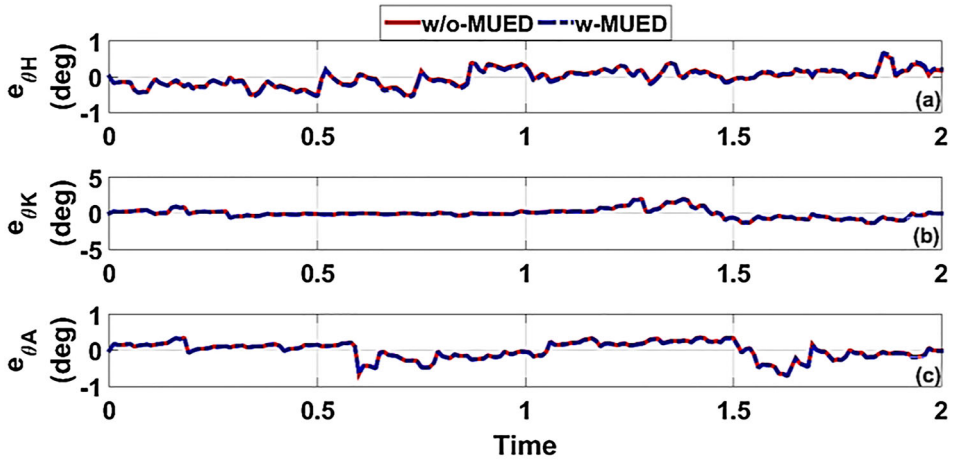

Figure 9. Simulation results of (a) hip, (b) knee, and (c) ankle joint tracking error for proposed control without and with MUED.

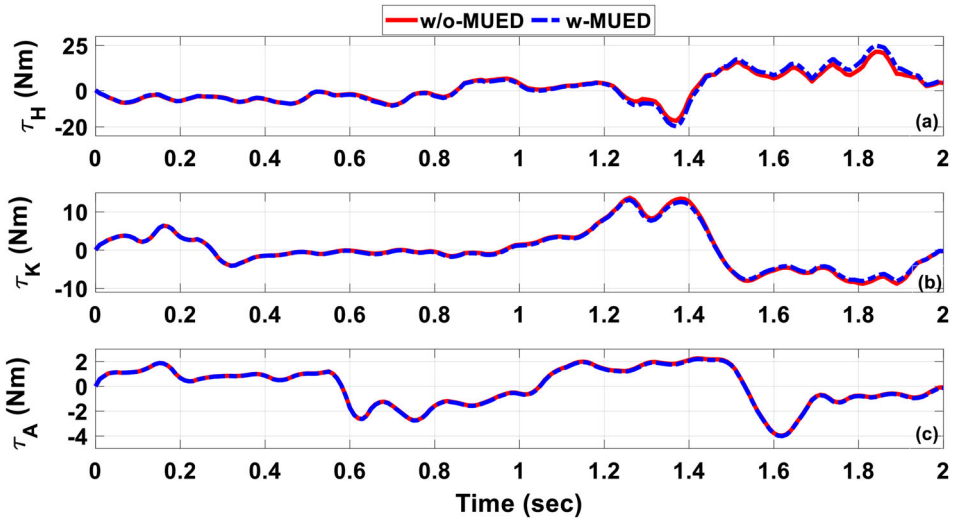

Figure 10. Simulation results of (a) hip, (b) knee, and (c) ankle joint control torques for proposed control without and with MUED.

control. Therefore, the robustness of the proposed control is validated for the lower limb exoskeleton system dynamics with model uncertainties and external disturbances.

Furthermore, the performance of RABS control is compared with the DMSA-PD control strategy. The details of the contrast control are presented here briefly. In the DMSA-PD control scheme, the gains of classical PD controller ($\boldsymbol{K}_p, \boldsymbol{K}_d$) are time-varying in nature and depend on the local-decentralized method [41]. The adaptive control gains ($\boldsymbol{K}_p(t), \boldsymbol{K}_d(t)$) are expressed as the addition of proportional and integral components, as follows:

$$\boldsymbol{K}_p(t) = \boldsymbol{K}_{pp}(t) + \int \dot{\boldsymbol{K}}_{pi}(t)dt \tag{41}$$

and,

$$\boldsymbol{K}_d(t) = \boldsymbol{K}_{dp}(t) + \int \dot{\boldsymbol{K}}_{di}(t)dt \tag{42}$$

where, $\boldsymbol{K}_{pp}(t) = diag(e_{\theta m}^2\ \boldsymbol{\Lambda}_{pp})$, $\boldsymbol{K}_{dp}(t) = diag(\dot{e}_{\theta m}^2\ \boldsymbol{\Lambda}_{dp})$ and,

$$\dot{\boldsymbol{K}}_{pi}(t) = diag(e_{\theta m}^2 \boldsymbol{\Lambda}_{pi} - \beth_p \boldsymbol{K}_{pi}(t)),$$

$$\dot{\boldsymbol{K}}_{di}(t) = diag(\dot{e}_{\theta m}^2 \boldsymbol{\Lambda}_{pi} - \beth_d \boldsymbol{K}_{di}(t))$$

Incorporating adaptive laws from Equations (41) and (42) in the PD controller, system torque can be estimated as:

$$\boldsymbol{\tau}' = \boldsymbol{\tau}_{act(DMSAPD)} = \boldsymbol{K}_p(t)\ e_{\theta m} + \boldsymbol{K}_d(t)\dot{e}_{\theta m} \tag{43}$$

In the above expressions, the joint angular error and rate of joint angular error derived from the reference (ideal) model are denoted by $e_{\theta m}$ and $\dot{e}_{\theta m}$, respectively. The reference model can be chosen as a second-order transfer function with desired performance characteristics. $\boldsymbol{\Lambda}_{pp}$, $\boldsymbol{\Lambda}_{dp}$, $\boldsymbol{\Lambda}_{pi}$, and $\boldsymbol{\Lambda}_{di}$ are the control adaptation parameters tuned by numerical iterations. $\beth_p$ and $\beth_d$ signify the positive coefficients of small value to nullify the diverging effects of the integral control gains.

For tracking the desired trajectory, the performance of the proposed control strategy (RABS) is investigated by computing the root mean square error (RMSE), and the improvement change while comparing with the

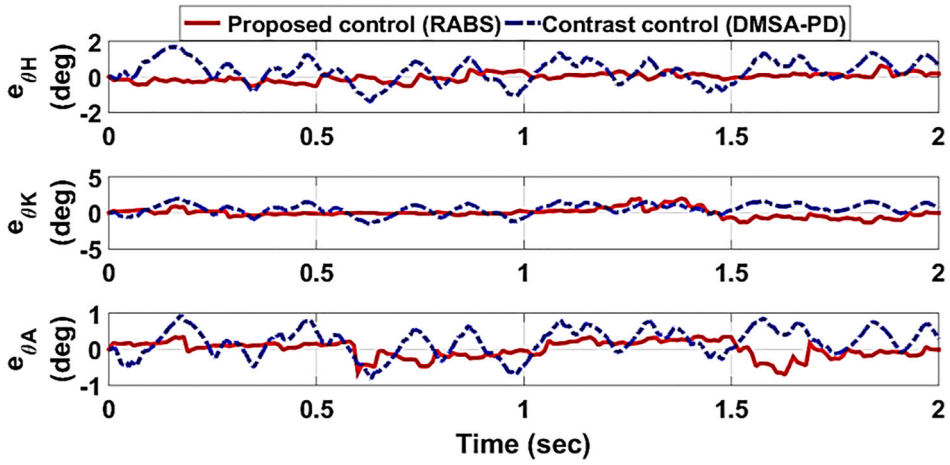

Figure 11. Simulation results of (a) hip, (b) knee, and (c) ankle joint tracking error for proposed control and contrast control without MUED.

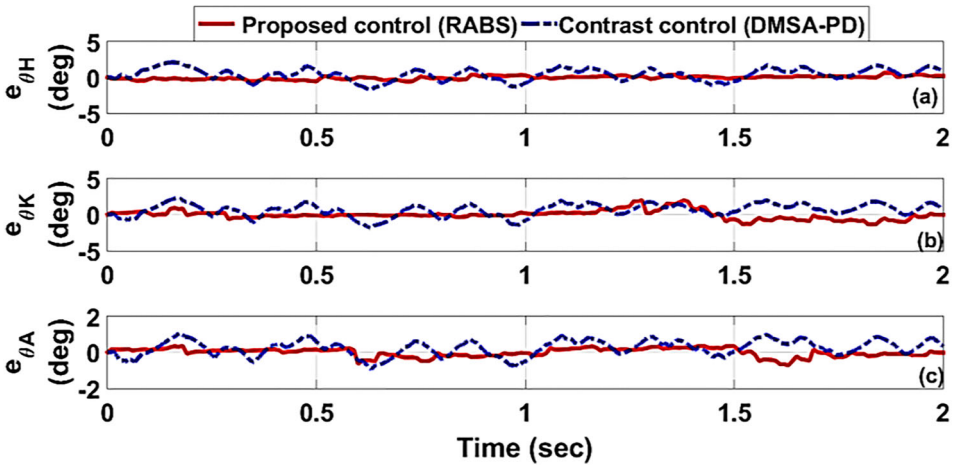

Figure 12. Simulation results of (a) hip, (b) knee, and (c) ankle joint tracking error for proposed control and contrast control with MUED.

contrast control performance is estimated by performance improvement index (PII), given as follows.

$$RMSE = \sqrt{\frac{1}{N}\sum_{q=1}^{N} ||e_q||^2} \tag{44}$$

$$PII = \frac{RMSE_{DMSAPD} - RMSE_{RABS}}{RMSE_{DMSAPD}} \times 100\% \tag{45}$$

where, $e_q : e_\theta$ is the angular deviation between desired and actual joint angles of the lower limb, and N denotes the size of the deviation vector. $RMSE_{DMSAPD}$ and $RMSE_{RABS}$ refer to the root mean square error associated with DMSA-PD control and RABS control strategy.

Considering the original system without any model uncertainties and external disturbances (w/o-MUED), the joint angular errors ($e_{\theta H}, e_{\theta K}$, and $e_{\theta A}$) from the proposed control are compared with the contrast control, as shown in Figures 11(a)–(c). The value of $RMSE_{DMSAPD}$ and $RMSE_{RABS}$ for the hip joint is found to be 0.096° and 0.031°, respectively. For the knee joint, the RMSE values are recorded as 0.121° and 0.083° for proposed and contrast control, respectively. The respective RMSE values for the ankle joint are observed to be 0.06° and 0.03°. On the other hand, for the system with model uncertainties and external disturbances (w-MUED), the joint angular errors obtained from both the control strategies are shown in Figure 12(a)–(c). The value of $RMSE_{DMSAPD}$ and $RMSE_{RABS}$ for the hip joint are found to be 0.121° and 0.033°, respectively. The RMSE values for the knee joint are obtained as 0.154° and 0.087°, respectively. For the ankle joint, the corresponding RMSE values are recorded as 0.071° and 0.031°.

The performance improvement index (PII) of the proposed control over the contrast control is shown in Table 4. It can be easily observed from Table 2; the proposed control is tracking the desired gait trajectory better than the contrast control for passive-assist rehabilitation of the lower limb. Moreover, in case-II, the increased values of PII by 5%, 12%, and 6% for hip, knee, and ankle joint confirm the better tracking potential of proposed control over contrast control in the presence of model uncertainties and external disturbances. This performance analysis further ensures

Table 4. Comparative performance analysis of proposed control.

Case I: System w/o-MUED			
Joint Name	RMSE (DMSAPDC), (deg.)	RMSE (RABSC), (deg.)	PII (%)
Hip	0.096	0.031	67.77
Knee	0.121	0.083	31.40
Ankle	0.06	0.03	50.00
Case II: System w-MUED			
Joint Name	RMSE (DMSAPDC), (deg.)	RMSE (RABSC), (deg.)	PII (%)
Hip	0.121	0.033	72.72
Knee	0.154	0.087	43.50
Ankle	0.071	0.031	56.33

that the exoskeleton system can effectively perform repetitive motions with desired gait trajectory during rehabilitation exercises.

The implication of the proposed control can be effectively appreciated in the case of post-stroke subjects with pathological gait. The potential end-users of the control-aided rehabilitation experiment could be the pediatric subjects, the age range of 8–12 years (25–40 kg and 115–125 cm), suffering from distorted gait post-paraplegic cerebral palsy with no sign of pain and discomfort (FMA ordinal scale 1). In the future, the simulation results of the proposed control work will be verified experimentally for the training duration of 3–4 gait cycles (each cycle of 2 s). Thereafter, the motion capture system would be installed again to estimate the biomechanical joint angles while wearing the exoskeleton and compared with healthy joint angles as estimated earlier. Based on the disparity between joint angles with and without exoskeletons and the subject's feedback, the tuning of the designed controller can be carried out for the end-users. The clinical investigation at the expense of the proposed controller will be explored in the near future.

6. Conclusions

This work has designed a new robust adaptive backstepping control for the lower limb exoskeleton system. The dynamic modelling of a coupled human-exoskeleton system has been presented for passive-assist gait rehabilitation of human children (children of 08–12 years age, 25–40 kg weight, and 115–125 cm height). The proposed control scheme has been designed with a virtual adaptation law to deal with model uncertainties and external disturbances. The Lyapunov theory has been formulated to ensure the system's stability during walking. The virtual control law has been selected without dynamical system parameters, leading to avoidance of "explosion of terms". The novel application of the proposed control has been carried out for considered exoskeleton systems without and with model uncertainties and external disturbances. The control system's input parameters are considered for a child with 10 years old, 28 kg weight, and 120 cm height. A motion analysis experiment, based on Kinect-LabVIEW, has been carried out to estimate the desired joint angles and trajectory during normal walking. At last, the performance of the designed control has been compared with contrast control, decentralized modified simple adaptive control, by evaluating root mean square error and performance improvement index while tracking the desired joint angles of the lower limb. From the experimental readings and simulation results, it can be easily perceived that the proposed control strategy shows improved performance for tracking the desired trajectory during passive-assist gait rehabilitation.

Acknowledgments

The authors acknowledge the Department of Scientific and Industrial Research, India, for establishing the PRISM (Promoting Innovations in Individuals, Start-ups, and MSMEs) scheme under which this project work is carried out.

Disclosure statement

No potential conflict of interest was reported by the author(s).

ORCID

Jyotindra Narayan http://orcid.org/0000-0002-2499-6039
Mohamed Abbas http://orcid.org/0000-0003-0813-7055
Santosha K. Dwivedy http://orcid.org/0000-0001-6534-8989

References

[1] Rudd AG, Bowen A, Young GR, et al. The latest national clinical guideline for stroke. Clin Med. 2017;17(2):154.
[2] World Health Organization. Global health estimates 2016: deaths by cause, age, sex, by country and by region, 2000-2016. Geneva: WHO; 2018.
[3] Langhorne P, Coupar F, Pollock A. Motor recovery after stroke: a systematic review. Lancet Neurol. 2009;8(8):741–754.
[4] Probosz K, Wcislo R, Otfinowski J, et al. A multimedia holistic rehabilitation method for patients after stroke. Annual Review of Cybertherapy and Telemedicine. 2009;7:261–263.
[5] Cheng L, Chen M, Li Z. Design and control of a wearable hand rehabilitation robot. IEEE Access. 2018;6:74039–74050.
[6] Qiu S, Wang Z, Zhao H, et al. Using body-worn sensors for preliminary rehabilitation assessment in stroke victims with gait impairment. IEEE Access. 2018;6:31249–312558.
[7] Gupta A, Singh A, Verma V, et al. Developments and clinical evaluations of robotic exoskeleton technology for human upper-limb rehabilitation. Adv Robot. 2020;2020:1–8.
[8] Chen B, Zhong CH, Zhao X, et al. Reference joint trajectories generation of CUHK-EXO exoskeleton for system balance in walking assistance. IEEE Access. 2019;7:33809–33821.
[9] Rupal BS, Rafique S, Singla A, et al. Lower-limb exoskeletons: research trends and regulatory guidelines in medical and non-medical applications. Int J Adv Rob Syst. 2017;14(6). doi:10.1177/1729881417743554.

[10] Kalita B, Narayan J, Dwivedy SK. Development of active lower limb robotic-based orthosis and exoskeleton devices: a systematic review. Int J Soc Robot. 2021;13(4):775–793.
[11] Zoss AB, Kazerooni H, Chu A. Biomechanical design of the Berkeley lower extremity exoskeleton (BLEEX). IEEE/ASME Trans Mechatron. 2006;11(2):128–138.
[12] Veneman JF, Kruidhof R, Hekman EE, et al. Design and evaluation of the LOPES exoskeleton robot for interactive gait rehabilitation. IEEE Trans Neural Syst Rehabil Eng. 2007;15(3):379–386.
[13] Kim JH, Han JW, Kim DY, et al. Design of a walking assistance lower limb exoskeleton for paraplegic patients and hardware validation using CoP. Int J Adv Rob Syst. 2013;10(2):113.
[14] Cestari M, Sanz-Merodio D, Arevalo JC, et al. ARES, a variable stiffness actuator with embedded force sensor for the ATLAS exoskeleton. Industrial Robot: An International Journal. 2014;41:518–526.
[15] Ouyang X, Ding S, Fan B, et al. Development of a novel compact hydraulic power unit for the exoskeleton robot. Mechatronics (Oxf). 2016;38:68–75.
[16] Tovar-Estrada M, Rodriguez-Liñan A, Quiroz G. Implementation of a scale-lab lower-limb exoskeleton with motion in three anatomical planes. Cybern Syst. 2019;50(6):516–538.
[17] Kwa HK, Noorden JH, Missel M, et al. Development of the IHMC mobility assist exoskeleton. In: 2009 *IEEE international conference on robotics and automation*. IEEE; 2009, May. p. 2556–2562.
[18] Esquenazi A, Talaty M, Packel A, et al. The ReWalk powered exoskeleton to restore ambulatory function to individuals with thoracic-level motor-complete spinal cord injury. Am J Phys Med Rehabil. 2012;91(11):911–921.
[19] Sanz-Merodio D, Sancho J, Pérez M, et al. 2017. Control architecture of the ATLAS 2020 lower-limb active orthosis. In: Tokhi Mohammad O , Virk Gurvinder S., editors. *Advances in cooperative robotics* (pp. 860–868. London, UK: World Scientific.
[20] Kazerooni H, Steger R, Huang L. Hybrid control of the Berkeley lower extremity exoskeleton (BLEEX). Int J Rob Res. 2006;25(5):561–573.
[21] Hussain S, Xie SQ, Jamwal PK. Control of a robotic orthosis for gait rehabilitation. Rob Auton Syst. 2013;61 (9):911–919.
[22] Yang P, Zhang G, Wang J, et al. Command filter backstepping sliding model control for lower-limb exoskeleton. Math Probl Eng. 2017;2017:1–10.
[23] Zhang X, Wang H, Tian Y, et al. Model-free based neural network control with time-delay estimation for lower extremity exoskeleton. Neurocomputing. 2018;272:178–188.
[24] Khan SG, Tufail M, Shah SH, et al. Reinforcement learning based compliance control of a robotic walk assist device. Adv Robot. 2019;33(24):1281–1292.
[25] Gui K, Tan UX, Liu H, et al. A new impedance controller based on nonlinear model reference adaptive control for exoskeleton systems. Int J Humanoid Rob. 2019;16(05):1950020.
[26] Mokhtari M, Taghizadeh M, Mazare M. Impedance control based on optimal adaptive high order super twisting sliding mode for a 7-DOF lower limb exoskeleton. Meccanica. 2021;56(3):535–548.
[27] Chen Z, Guo Q, Yan Y, et al. Model identification and adaptive control of lower limb exoskeleton based on neighborhood field optimization. Mechatronics (Oxf). 2022;81:102699.
[28] Mokhtari M, Taghizadeh M, Mazare M. Robust and adaptive control of an exoskeleton robot for tracking modified desired trajectory based on zero moment point stability theory. Amirkabir J Mechanical Engineering. 2022;53(12):13–13.
[29] Mokhtari M, Taghizadeh M, Ghanbari PG. Fault tolerant control based on backstepping nonsingular terminal integral sliding mode and impedance control for a lower limb exoskeleton. Proceedings of the Institution of Mechanical Engineers. Part C: Journal of Mechanical Engineering Science. 2022;236(6):2698–2713.
[30] Narayan J, Kumar Dwivedy S. 2021. Preliminary design and development of a low-cost lower-limb exoskeleton system for paediatric rehabilitation. Proceedings of the Institution of Mechanical Engineers, Part H: Journal of Engineering in Medicine, doi:10.1177/09544119219 94940.
[31] van den Bogert AJ, Read L, Nigg BM. An analysis of hip joint loading during walking, running, and skiing. Med Sci Sports Exercise. 1999;31(1):131–142.
[32] Weinhandl JT, Irmischer BS, Sievert ZA. Effects of gait speed of femoroacetabular joint forces. Appl Bionics Biomech. 2017;2017:1–7.
[33] Narayan J, Abbas M, Dwivedy SK. Transpose Jacobian control of flexible joint upper limb exoskeleton system. In: Kumar R, Chauhan VS, Talha M, et al, editors. Machines, mechanism and robotics. lecture notes in mechanical engineering. Singapore: Springer; 2022. p. 401–411.
[34] Folęga P, Siwiec G. Numerical analysis of selected materials for flexsplines. Arch Metall Mater. 2012;57: 185–191.
[35] Ueura K, Slatter R. Development of the harmonic drive gear for space applications. European Space Agency-Publications-ESA SP. 1999;438:259–264.
[36] Grainer KnowHow. Types of belt drives and how they improve efficiency, https://www.grainger.com/know-how/equipment-information/kh-types-of-belt-drives-efficiency, accessed on 15 Sep. 2021.
[37] Spong MW, Hutchinson S, Vidyasagar M. Robot modeling and control. New York (NY): Wiley; 2006.
[38] Zhou J, Wen C. Adaptive backstepping control of uncertain systems: nonsmooth nonlinearities, interactions or time-variations. City: Springer; 2008.
[39] Abbas M, Al Issa S, Dwivedy SK. Event-triggered adaptive hybrid position-force control for robot-assisted ultrasonic examination system. Journal of Intelligent & Robotic Systems. 2021;102(4):1–19.
[40] Narayan J, Dwivedy SK. Biomechanical study and prediction of lower extremity joint movements using Bayesian regularization-based backpropagation neural network. J Comput Inf Sci Eng. 2021;22(1):014503.
[41] Ulrich S, Sasiadek JZ. Decentralized simple adaptive control of nonlinear systems. Int J Adapt Control Signal Process. 2014;28(7-8):750–763.

Appendix A

$$\begin{cases} M_{11} = m_1 l_{c1}^2 + I_1 + m_2(l_1^2 + l_{c2}^2 + 2l_1 l_{c2}\mathbb{C}_2) + I_2 \\ \quad +m_3(l_1^2 + l_2^2 + l_{c3}^2 + 2l_1 l_2 \mathbb{C}_2 + 2l_1 l_{c3}\mathbb{C}_{23}) + I_3 \\ M_{12} = m_2(l_{c2}^2 + l_1 l_{c2}\mathbb{C}_2) + I_2 \\ \quad +m_3(l_2^2 + l_{c3}^2 + l_1 l_2 \mathbb{C}_2 + l_1 l_{c3}\mathbb{C}_{23} + 2l_2 l_{c3}\mathbb{C}_3) + I_3 \\ M_{13} = m_3(l_{c3}^2 + l_1 l_{c3}\mathbb{C}_{23} + l_2 l_{c3}\mathbb{C}_3) + I_3 \\ M_{22} = m_2 l_{c2}^2 + I_2 + m_3(l_2^2 + l_{c3}^2 + 2l_2 l_{c3}\mathbb{C}_3) + I_3 \\ M_{23} = m_3(l_{c3}^2 + l_2 l_{c3}\mathbb{C}_3) + I_3 \\ M_{33} = m_3 l_{c3}^2 + I_3 \\ M_{21} = M_{12}, M_{13} = M_{31}, M_{23} = M_{32} \end{cases} \tag{A1}$$

$$\begin{cases} C_{11} = -2m_2 l_1 l_{c2} S_2 \dot{\theta}_2 \\ \quad -2m_3 l_1 l_2 S_2 \dot{\theta}_2 - 2m_3 l_1 l_{c3} S_{23}(\dot{\theta}_2 + \dot{\theta}_3) - 2m_3 l_2 l_{c3} S_3 \dot{\theta}_3 \\ C_{12} = -m_2 l_1 l_{c2} S_2 (2\dot{\theta}_1 + \dot{\theta}_2) - m_3 l_1 l_2 S_2 (2\dot{\theta}_1 + \dot{\theta}_2) \\ \quad -m_3 l_1 l_{c3} S_{23}(2\dot{\theta}_1 + \dot{\theta}_2 + \dot{\theta}_3) \\ C_{13} = -m_3 l_1 l_{c3} S_{23}(2\dot{\theta}_1 + 2\dot{\theta}_2 + \dot{\theta}_3) \\ C_{21} = -2m_3 l_2 l_{c3} S_3 \dot{\theta}_3 + (m_2 l_1 l_{c2} S_2 \\ \quad +m_3(l_1 l_2 S_2 + l_1 l_{c3} S_{23}))\dot{\theta}_1 \\ C_{22} = -2m_3 l_2 l_{c3} S_3 \dot{\theta}_3 \\ C_{23} = -m_3 l_2 l_{c3} S_3 (2\dot{\theta}_1 + 2\dot{\theta}_2 + \dot{\theta}_3) \\ C_{31} = m_3 l_1 l_{c3} S_{23} \dot{\theta}_1 + m_3 l_2 l_{c3} S_3 (\dot{\theta}_1 + 2\dot{\theta}_2) \\ C_{32} = m_3 l_2 l_{c3} S_3 (2\dot{\theta}_1 + \dot{\theta}_2) \\ C_{33} = 0 \end{cases} \tag{A2}$$

$$\begin{cases} G_1 = m_1 g l_{c1} S_1 + m_2 g(l_1 S_1 + l_{c2} S_{12}) \\ \quad +m_3 g(l_1 S_1 + l_2 S_{12} + l_{c3} S_{123}) \\ G_2 = m_2 g l_{c2} S_{12} + m_3 g(l_2 S_{12} + l_{c3} S_{123}) \\ G_3 = m_3 g l_{c3} S_{123} \end{cases} \tag{A3}$$

In (A1–A3), $\mathbb{C}_a = \cos(\theta_a), \mathbb{C}_{ab} = \cos(\theta_a + \theta_b), \mathbb{C}_{abc} = \cos(\theta_a + \theta_b + \theta_c), S_a = \sin(\theta_a), S_{ab} = \sin(\theta_a + \theta_b), S_{abc} = \sin(\theta_a + \theta_b + \theta_c)$; for $a = 1, 2, 3$, $b = 1, 2, 3$ and $c = 1, 2, 3$. I_i denotes the moment of inertia about the ith link. The total mass of the coupled i-th link is $m_i = m_i^e + m_i^h$ where superscript notations (e) and (h) imply the meaning of exoskeleton and human, respectively.